

# Electromagnetic Tomography: Real-Time Imaging using Linear Approaches

Caeiros, J. M. S. and Martins, R. C.

October 17, 2010

## Abstract

The objective of the present work is to apply linear image reconstruction algorithms specifically to two tomographic imaging technologies aimed for biomedical applications, the Magnetic Induction Tomography (MIT) and the Electrical Impedance Tomography (EIT). This required the implementation of numerical forward problem solvers, which simulate the interaction between a given electromagnetic field and a body with a specific conductivity distribution. They are intended to be fully automatic, requiring only the specification of the problem data, and make it easy the integration of the measurements, which are subsequently used in the image reconstruction process.

In terms of image reconstruction, different reconstruction algorithms were studied in order to get images in real-time. The Back-Projection and the Filtered Back-Projection methods were implemented, either along straight lines, or along magnetic flux lines (specifically for the MIT) or equipotential lines (specifically for EIT). Still regarding the EIT image reconstruction, the applicability of the developed 2D forward problem solver to a state of the art linear reconstruction algorithm (GREIT), originally based on a 3D forward problem solver, was studied.

The results obtained were satisfying in the sense that they demonstrate the applicability of these technologies to the clinical environment.

**Key Words:** Magnetic Induction Tomography, Electrical Impedance Tomography, Finite Integration Technique, Filtered Back-Projection, GREIT.

---

## 1 Introduction

There is a great deal of information within the bioimpedance map of the body. It includes the characterization and identification of cells based on their impedance, which differs between cells based on the size, orientation, and membrane thickness, among other factors. Also, changes in this map translate to specific physiological and/or pathological conditions. For instance, the measured impedance is highly dependent on the amount of water in the body and

hence this information can be used to detect edemas. Another example is the identification and characterization of cancer cells, since they exhibit different impedances when compared to healthy tissues. Electromagnetic tomography intends to explore these phenomena, using the impedance information of the different tissues to form images of the contents of the human body.

Magnetic induction tomography is a non-invasive and contact-less electromagnetic imaging technology used to map the passive electromagnetic prop-

erties of an object under investigation. Harmonic signals with frequencies between tens of kHz to 1 MHz -10 MHz (e.g. [1], [2]) are applied in excitation coils in order to generate an oscillating primary magnetic field, which in turn induces eddy currents on the object. The secondary magnetic field generated by these currents carries the information about the complex conductivity distribution inside the object. It contains a component produced by conduction currents proportional to the frequency and in quadrature with the primary field and an in phase component, proportional to the square of the frequency, caused by displacement currents. It induces a change of magnitude and phase of the primary field. Most linear approaches, as the ones explored in this work, use only the phase shift information to reconstruct the impedance map of the object ([1]), whereas the non-linear methods use both ([3, 4]).

The MIT inverse problem can be seen as a soft field parameter estimation problem, which means that the underlying physical phenomenon is ruled by a set of electromagnetic partial differential equations (PDE) and the parameters to be inferred are the material coefficients. It's an ill-posed and non-linear estimation problem in its full set of unknown variables, fields and conductivity map, which uses several measurements of electromotive forces induced in sensing coils around the object, for different source positions. The number of independent acquisitions should be large in order to reduce the ill-posedness of the problem.

Special attention has recently been given to the biomedical application of this technology (e.g. [1, 2]), mainly due to its low cost, contactless nature, the fact that it is inherently safe and its good penetration in biological tissues, including bone. However, there is still a lot of ground to be covered before its clinical application, namely the improvement of the spatial resolution and the signal and contrast to noise ratios.

Electrical Impedance Tomography is a non-invasive tomographic imaging technique involving the formation of images of the impedance distribution across a sectional plane of a body under test, from peripheral electrical measurements. It is the most

developed case of electromagnetic tomography, with commercial systems already available.

EIT can generally be seen as the inverse, ill-posed and non-linear problem of determining the impedance in the interior of a bounded, simply connected domain, given simultaneous measurements of direct or alternating electric currents and voltages at its boundary, being ruled as well by a set of electromagnetic PDE.

According to [5], the typical EIT system consists of an array of  $N$  electrodes placed around the periphery of the body under investigation. Small amplitude electrical currents (1-10 mA) at a fixed frequency are applied in turn to each pair of electrodes, known as drive pairs. For each one, the electric potential is measured by the remaining ( $N-3$ ) pairs electrodes, named receive pairs, in a differential manner.

The typical EIT system is capable of producing difference imaging [6]. It consists on the measurement of two different data sets, at different times or frequencies. These are then subtracted (difference EIT), or subtracted and then divided (normalized difference EIT) by a reference set of measurements corresponding to the background conductivity. The resulting images translate to changes in the background conductivity, representing a given physiological parameter, such as blood volume or cell size.

There are three main electrical current injection protocols ([7]), which are classified into adjacent, opposite and adaptive. The first one was devised in 1987 by Brown and Segar [6] in which the current is applied by an adjacent drive pair and the voltage is measured from all other adjacent receiving pairs. This is the injection protocol used during the course of this work, as it is the one on which most linear image reconstruction methods are based. However, it is advisable to use different combinations of drive and receiver pairs in order to increase the size of independent data, thus reducing the ill-posedness of the problem and improving the image spatial resolution [8].

There are two methods to model electrodes computationally in EIT [9]. The first one, which was used in this work, consists in approximating the current

density by a constant on the surface of each electrode, and zero in the spaces between electrodes. For a more accurate model, one should use the so called complete electrode model, which considers the current density as a function of the electrode geometry and its contact impedance.

## 2 The forward Problems

A forward model describes the physical laws that characterize the system. In this case, its implementation enables the simulation of the interaction of a given electromagnetic field with a body with specific conductivity distribution, thus creating a set of virtual measurements that are afterwards used to infer that same conductivity distribution.

Several assumptions are taken in the implemented electromagnetic model. The first is isotropy of the complex conductivity, which reduces the ill condition of the problem. Although not real in a biological sense [10], it is used in most of the published works (e.g. [4]). Constant magnetic permeability is also considered. Although not entirely true, it is a valid assumption when biological bodies are concerned since the magnetic permeability variability between tissues isn't great and its effect isn't as preponderant as the effect of the complex conductivity. Finally, the harmonic and stationary scenario is used.

### 2.1 Mathematical Formulations

For the MIT case, the used formulation is based on the magnetic vector potential,  $\vec{A}$ , separated in its source component,  $\vec{A}_s$ , and residual component, originated from the eddy currents in the material,  $\vec{A}_r$ , and the modified electric scalar potential,  $\phi$ . The Ampère's law and the continuity equation for the harmonic and stationary case, written in terms of these potentials, render a robust and numerically stable system of equations [11], given by:

$$\frac{1}{\mu} \Delta \vec{A}_r - i\omega \bar{\sigma} (\nabla \phi + \vec{A}_r) = i\omega \bar{\sigma} \vec{A}_s, \quad (1)$$

$$\nabla \cdot [i\omega \bar{\sigma} (\nabla \phi + \vec{A}_r)] = -i\omega \nabla \cdot \bar{\sigma} \vec{A}_s. \quad (2)$$

Equation (2) enforces the normal component of the current density in the interface between a conducting and nonconducting region to be null. Nevertheless, a homogeneous Dirichlet boundary condition needs to be imposed at the space boundary, forcing the normal component of  $\vec{B}_r$  to be null.

The formulation used for EIT is based solely on the electric scalar potential,  $V$ , under the approximation to the quasi-static state [9]. The governing equation is derived from the continuity equation and is expressed as follows,

$$\nabla \cdot \sigma \nabla V = -\frac{\partial \rho}{\partial t}. \quad (3)$$

Using this formulation one only has to place several charge sources and sinks at the boundary of the object under analysis, taking care to obey the law of conservation of current, and apply homogeneous Dirichlet boundary conditions at the space boundary. This formulation leads to a non-singular system of equations and the rendered solution for the potential is unique [9].

### 2.2 Discretization Method

The method chosen to perform the discretization of the governing equations of both MIT and EIT was the Finite Integration Technique (FIT) (e.g. [12, 13]). It allows proofing stability and conservation properties of discrete fields and is based on the application of the integral form of the Maxwell's equations to a set of dual staggered grids. In this work, orthogonal grids were implemented. For the MIT, due to the size of a 3D problem, it was necessary to implement a subgridding scheme. A new discretization method was developed that creates an octree type grid in a bottom up approach that automatically adapts itself to the problem geometry. It allows concentrating high resolution areas solely where they are needed, thus reducing the number of required cells to perform the space discretization, while maintaining the accuracy of the solution. In the case of EIT, since the problem was reduced to 2D, its size is considerably smaller and hence a regular grid with no subgridding regions

was used. In the FIT the electromagnetic quantities are substituted by their integrals along edges (*1-forms*), faces (*2-forms*) or volumes (*3-forms*) of the cells composing the dual grid complex. According to the notation presented in [12], the magnetic vector potential is a *1-form* and is expressed by  $\hat{a}$ , whereas the standard and modified electric scalar potentials are *3-forms* and are simply represented by  $V$  and  $\phi$ , respectively. Assuming a lexicographical ordering of the cells composing the main grid, the discrete electromagnetic quantities can be assembled into column vectors and the classic differential operators can be defined as matrices containing only topological information on the incidence relation of the cells within the grid complex and on their orientation. These discrete topological operators can then be applied to the electromagnetic quantities simply through matrix product. In order to distinguish the continuum case from the discrete one, the following notation is adopted: **lap** is the discrete laplacian operator, **grad** is the discrete gradient and **div** is the discrete divergence. They enable building the following discrete equations for MIT,

$$\mathbf{lap} \hat{a}_r - i\omega \mathbf{M}_\sigma (\mathbf{grad} \phi + \hat{a}_r) = i\omega \mathbf{M}_\sigma \hat{a}_s, \quad (4)$$

$$\mathbf{div} [i\omega \mathbf{M}_\sigma (\mathbf{grad} \phi + \hat{a}_r)] = -\mathbf{div} [i\omega \mathbf{M}_\sigma \hat{a}_s], \quad (5)$$

where  $\mathbf{M}_\sigma$  is a diagonal matrix containing the information about the conductivity of each cell. Equations (4) and (5) form a system of equations, whose size is  $(3N + N') \times (3N + N')$ ,  $N$  being the number of elements composing the grid and  $N'$  the number of non-zero conductivity cells. The source field is calculated using a discretization of the Biot-Savart law and the system is solved using the biconjugate gradient stabilized method based on preconditioning through an incomplete LU factorization.

Concerning the EIT, its discretized governing equations are given by,

$$\mathbf{div} [P\sigma \mathbf{grad} u] = -\frac{d\rho}{dt}. \quad (6)$$

The size of this system of equations is simply  $N$ , the number of cells required for the space discretization, and is solved through Gaussian elimination variants.

## 2.3 Results

The first set of results concern the MIT forward problem. Figure 1 presents a scenario in which both object and sensor regions have a solution with high accuracy. These are the cases used for simulation of measurements which are then going to be used to perform image reconstruction. In this figure, two possible subgridding schemes can be observed, both rendering a solution with the same accuracy. However, figure 1 a) is much more interesting and computationally effective, since it requires four times less cells to discretize the domain than in b), and takes the same amount of time to generate. This leads to a system of equations four times smaller which takes considerably less time to solve, making it a very important optimization tool for the MIT forward problem.

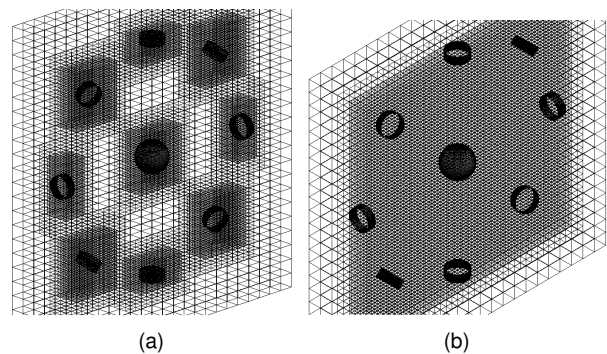


Figure 1: 3D mesh with three different resolution levels and a) 9 subgridding regions; b) a single subgridding region. 8 source/sensor coils and a sphere in the center of the space can also be observed.

The next figure represents an object that could actually be used as a conductivity phantom to evaluate, analyze, and tune the performance of an MIT system. It is intended to show the current distribution inside this complex object. The generated phantom presented in figure 2 (a) is based on the work published in [4] and consists in a large sphere with 5 cm of radius and a conductivity of 0.3 S/m, containing one spherical perturbation of 2 cm of radius and 1.5 S/m of conductivity and another one with 1 cm of radius and 0.05 S/m of conductivity. The phantom was placed in the center of the space and a source

coil composed by 15 windings of 2.5 cm of radius using a current of amplitude 2 A and frequency of 1 MHz was employed. In figures 2 (b) and (c) the amplitude of the eddy current density distribution is depicted in two different cross sections.

The first thing that should be noted is that the current density is confined to the limits of the object and no current circulates in nonconducting regions. Another interesting thing is that the maximum current density appears, as expected, in the highest conductivity region and that in the lowest conductivity sphere almost no current circulates. This differentiated distribution is what bestows the ability to reconstruct objects in an MIT system. In the same figure one can also observe regions inside the object where the current is nearly zero. They correspond to the axis of current circulation.

The results obtained using the 2D forward problem solver developed for EIT are presented in figure 3. They are based on a prototype composed by 16 equally spaced electrodes placed around the object [6]. For a given driving pair injecting current inside the object, the resulting electric potential is used to calculate current stream lines by computing its gradient and using the constitutive relation between the current density and the electric field. The adjacent and opposite current injection protocols were used.

In figure 3 (a), a circular object of radius 0.1 m and

conductivity of 1 S/m, withholding two circular perturbations, with higher (10 S/m) and lower (0.1 S/m) conductivities with respect to the medium can be observed. These values were chosen as such so the changes in the current and potential patterns could be visible (figures 3 (b) and (c)).

The most interesting thing that should be noted here is that the current is trying to flow through the lowest impedance path between the injecting and receiving electrodes. This phenomenon is well depicted in figure 3 c), where it can be seen that the current lines are clearly trying to enter the high conductivity perturbation and avoid the low conductivity one. This is in exact agreement with electromagnetic theory and gives credibility to the developed software.

### 3 The Inverse Problems

The image reconstruction process was addressed using linear approaches. The Back-Projection and filtered back projection methods were implemented, either along straight lines, or along magnetic flux lines (specifically for MIT) or along equipotential lines (specifically for EIT). The application of the GREIT, a state of the art image reconstruction algorithm based on the calculation of a sensitivity matrix, was also performed for EIT. The feasibility of its application using an underlying 2D forward problem was studied, in

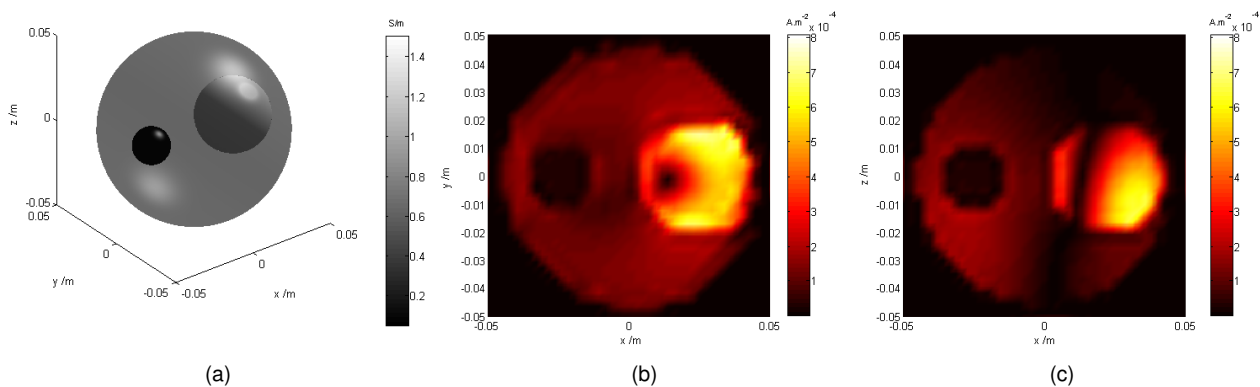


Figure 2: (a) 3D view of a conductivity phantom composed of a 0.3 S/m conductivity sphere, containing two others, one with a conductivity of 1.5 S/m and the other with 0.03 S/m. Absolute values of the current density distribution. (b) cross section along the plane  $x = 0$ ; (c) cross section along the plane  $z = 0$ .

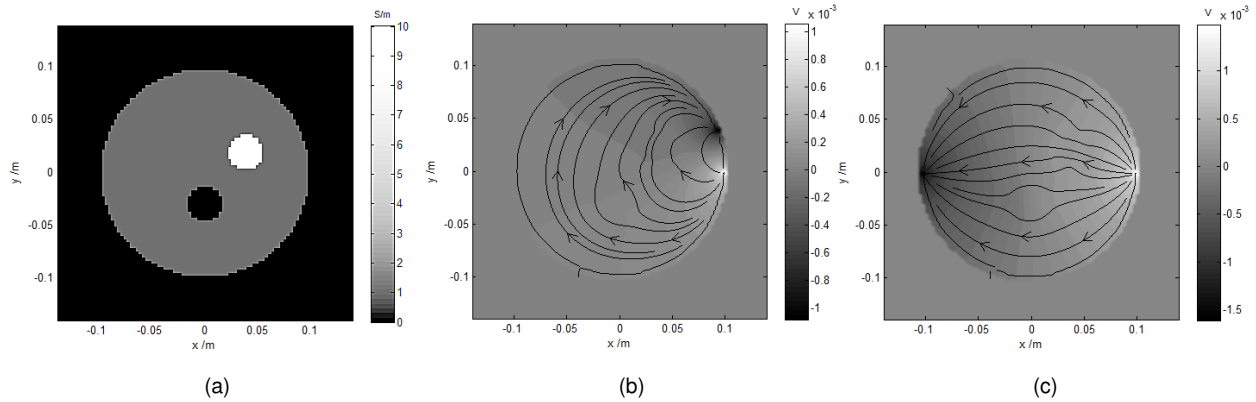


Figure 3: a) Conductivity phantom composed by a circular object of 1 S/m of conductivity and radius of 10 cm, containing two perturbations of 1.5 cm of radius and conductivity of 10 S/m and 0.1 S/m; Resulting electric scalar potential fields and current lines from b) adjacent and c) opposite current injection protocols.

contrast with the full 3D case presented in [14].

### 3.1 Back-Projection Methods

This class of image reconstruction algorithms rely on the usage of the Radon transform, that defines a projection  $p$  at a given angle  $\phi$ , as the ordered set of all ray-sums at a given position. These are defined as the weighted sum of the contributions of all the points of the conductivity distribution map that lie along the path of a ray connecting source and detectors. This transform is given, in polar coordinates  $(x', \phi)$ , by:

$$p_\phi(x') = \int_L f(x, y) dl, \quad (7)$$

where  $L$  describes the ray-path and  $f(x, y)$  stands for the density function representing the conductivity map. In MIT, the projections consist in phase shifts between source and detector signals, induced by the residual field, whereas in EIT they are a set of measured impedances.

The reconstruction technique consists in back-projecting each projection across the plane, i.e., assigning the magnitude of each ray-sum to every point that makes up the ray. The difference between the standard Back-Projection along straight lines and the modified versions used in MIT and EIT lies essentially in the parametrization of the ray path.

The simple Back-Projection method is inherently blurred. The usage of the Central Slice Theorem leads to the conclusion that this can be counteracted if the one-dimensional projections are properly filtered with a one-dimensional filter kernel. This defines the Filtered Back-Projection Method. The typical filters used include the Ram-Lak, Shepp-Logan, low-pass cosine or generalized Hamming.

### 3.2 GREIT

The Graz consensus Reconstruction algorithm for EIT (GREIT) [14] is a linear image reconstruction algorithm developed in 2009 specifically for EIT, namely for pulmonary imaging. The objective of this algorithm is to create a linear reconstruction matrix which converts a set of measurements into the corresponding conductivity distribution. Several figures of merit, such as uniform amplitude response, small and uniform position error, small ringing effect, uniform resolution, limited shape deformation and high resolution, while maintaining small noise amplification and small sensitivity to electrode and boundary movement, are directly incorporated in the reconstruction algorithm.

The desired reconstruction matrix is assembled by associating a set of training data consisting in small circular targets, with varying diameter, spread

randomly and uniformly throughout the image plane, with the respective measurements registered in the sensors. The training set should be much larger than the number of independent measurements in order to avoid training bias.

### 3.3 Results

Two different prototypes were tested in MIT. The first one consists in a single source and detector coils, sharing the same axis, translating and rotating together to obtain the required projections. The standard Filtered Back-Projection is used for image reconstruction. The second prototype uses a single source and multiple detectors, in which all axis belong to the same plane, stationed in the a ring surrounding the object. The projections are acquired by rotating the source and detectors by the same angle. The image is reconstructed by a modified Filtered Back-Projection along magnetic flux lines.

The first results intend to demonstrate the spatial sensitivity of a MIT system, i.e. the variation of the phase shifts with the spatial location of the object in relation to the position of both source and detector. For this purpose a single source and detector coils were used, sharing the same axis, which is parallel to the x axis, but 35 cm apart. The frequency in this case was 20 MHz and the test object consists in a sphere with diameter equal to 10 cm. To assess the effect of the conductivity in the acquired measurements, two homogeneous conductivity distributions were applied to the sphere, one equal to 7 S/m and the other equal to 3.5 S/m. Both source and detectors have fixed positions and the object is moved along the x axis or the y axis. The obtained results are displayed in figure 4.

The displayed curves are in agreement with the experimental findings published in [1]. One can see that the measured phase shifts are in direct proportion to the conductivity of the sphere. The behavior of the curves is also in accordance with the magnetic induction theory. The x-dependence curve shows a minimum phase shift when the object is equally distant from the source and detector, a global maximum

when the object is nearer the source and a local maximum when the object is closer to the detector. This can be explained by the relation between the magnitude of the induced magnetic field and the distance that it needs to travel in order to reach the detector. This contrasts with X-ray CT, where for a single source and detector, the object movement along the x axis would always render the same measurement.

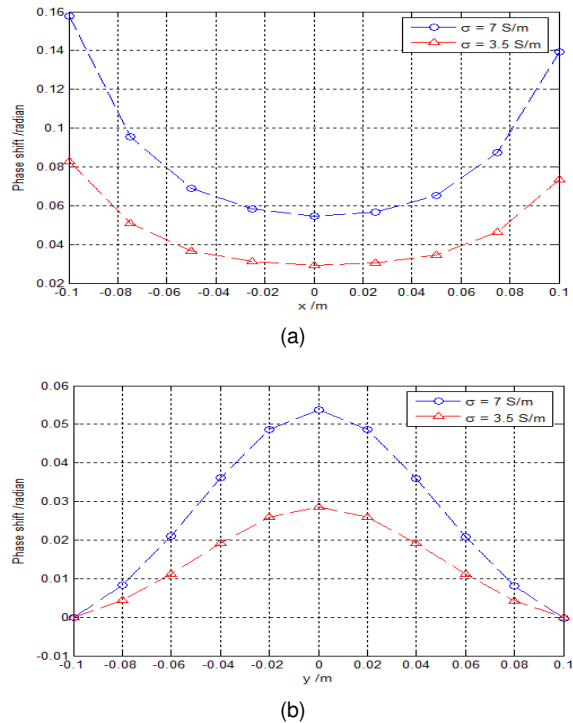


Figure 4: Dependence of the measured phase shifts on the position of the object along the (a) x axis and (b) y axis and on the object's conductivity.

The y-dependence curve confirms the fact that the sensitivity is higher in the zone nearer the magnetic line connecting inductor and detector. This is the main source of information required for image reconstruction through Filtered Back-Projection.

The next results show the difference between the standard Filtered Back-Projection method along straight lines and its modified version along magnetic flux lines. For that, two spheres were reconstructed, with radius of 2.5 cm but with different conductivities. One has 1 S/m of conductivity and its center has the coordinates (0.05,0,0) m, and the other has

0.7 S/m of conductivity and is stationed in the position  $(-0.05,0,0)$  m (figure 5 (a)). Since no noise was simulated, the Ram-Lak filter was employed.

One thing that should be noted is that there is a reconstructed conductivity zone connecting the two objects, that does not exist in the true conductivity map (see figure 5 (b) and (c)). This happens as a result of increased phase shifts due to the proximity of the object to the source or sensors. The projections taken around  $90^\circ$  will then be much larger in magnitude than the ones taken around  $0^\circ$  or  $180^\circ$ , and since their back-projection tracts cross the region between the two spheres, then a conductivity value will be assigned there which cannot be canceled by filtering. This effect is minimized in the modified Filtered Back-Projection, where there are fewer lines crossing the center of the image since now, due to the path of back-projection, the information is more concentrated in the periphery. Both methods enable the identification of the location of the spheres.

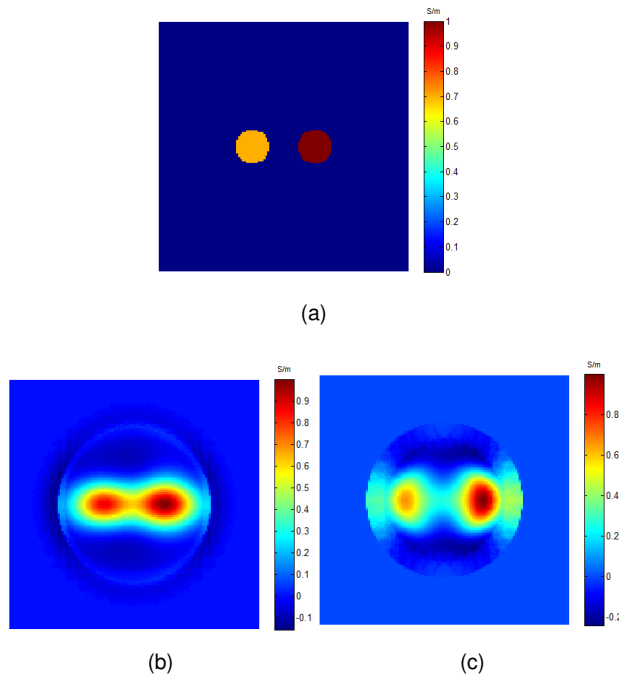


Figure 5: (a) True conductivity map; image reconstruction using the standard (b) and the modified (c) Filtered Back-Projection method. 36 projections were used.

The modified Filtered Back-Projection leads to a reconstruction with a better correspondence in terms of value to the true conductivity map than the standard one. Therefore it is the preferred method.

The last result for MIT corresponds to a conductivity phantom composed by an ellipsoid of 0.3 S/m of conductivity, 8 cm of radius in the x direction and 3 cm in the y and z directions, containing two spherical perturbations of radius 1.5 cm and conductivity of 1 S/m and 0.7 S/m (see figure 6 (a)). The image was reconstructed using the modified Filtered Back-Projection method, employing the ram-lak filter kernel and is displayed in figure 6 (b). Here it is visible the outline of the ellipsoid as well as two spherical perturbations. Although there is a good correspondence between the shape of the reconstructed phantom and the original one, in terms of conductivity they are slightly different, specially in the lower conductivity perturbation. This could somewhat be avoided if a reference data obtained for the ellipsoid without the spherical perturbations was used. It could be seen as a calibration step and it would lead to a result similar to the one presented in figure 5 (c), where only the perturbations would be visible.

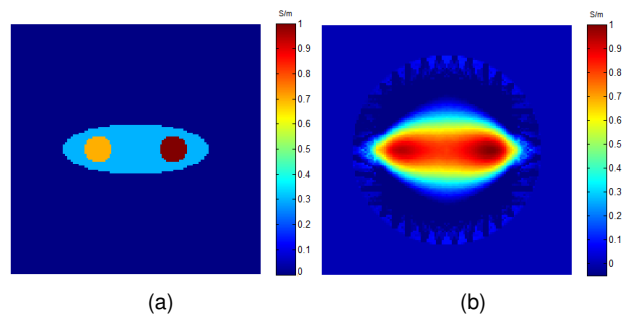


Figure 6: Image reconstruction of a conductivity phantom. (a) true map; (b) reconstruction.

Regarding the results obtained for EIT, the next set intends to compare the filtered Back-Projection algorithm along equipotential lines and GREIT. For that, two spherical perturbations were used, with lower and higher conductivities than the medium, and the 16 electrodes system was used to perform the required measurements. The original conductivity dis-

tribution is displayed in figure 7 (a), and the reconstructed ones in (b) and (c). The training set required by the GREIT is composed by 520 samples, which corresponds to five times the number of independent measurements of the system, and each sample target has 1.5 S/m of conductivity.

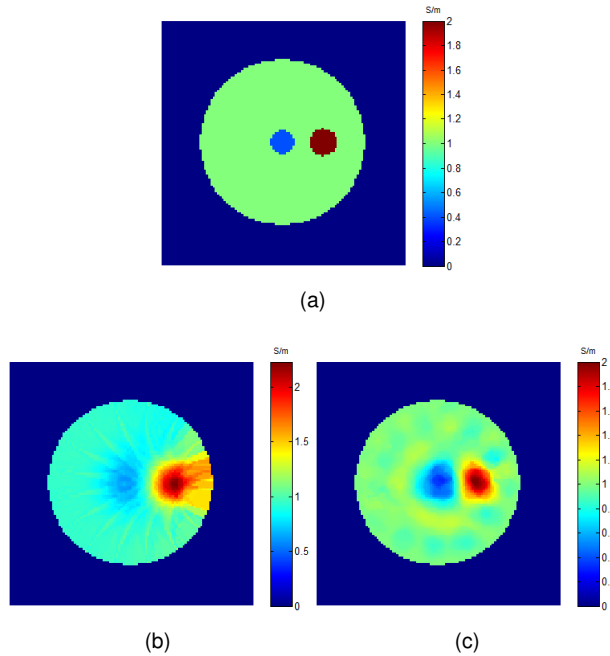


Figure 7: (a) Represents the true conductivity map; image reconstruction using (b) the Equipotentials Back-Projection method and (c) the GREIT.

It is obvious that the GREIT provides a result far superior to the one obtained through the Back-Projection method in terms of both image quality and correspondence between the reconstructed conductivities and the true ones. When multiple objects with different conductivities are present the Back-Projection method does not lead to satisfactory results. The location of the objects is still accurate but the reconstructed values are slightly different than the original ones. Also, similarly to what happened in the Back-Projection along magnetic field lines in MIT, the information is smeared towards the periphery. This is more visible in the case of the highest conductivity perturbation, where there is a reconstructed conductivity path connecting the object to the electrodes' region. None of this happens with GREIT. Minimum

blurring is present, the location of the objects is accurate, the correspondence between true and reconstructed conductivities is almost perfect, all of which make this method much more useful than the previous one.

The final result concerns only the GREIT and its behavior in the presence of a more complex conductivity distribution. Since the GREIT is designed for pulmonary imaging, a conductivity phantom inspired by [15] was designed. Elliptical domains are used to represent the heart and two lungs and the conductivities are chosen to simulate the conductivity distribution during systole. Hence, since blood was ejected from the heart to the lungs, their conductivities are respectively equal to 0.4 S/m and 1.75 S/m. The original conductivity map is depicted in figure 8 (a) and the reconstructed one in (b). The training data is the same as in the previous result.

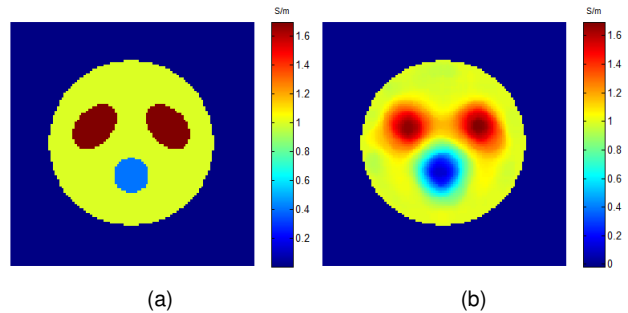


Figure 8: Image reconstruction of a conductivity phantom representing the heart and lungs. (a) true conductivity map, (b) reconstruction using the GREIT based on 520 training data samples.

In the reconstructed image one can clearly identify the three objects composing the phantom. Inside the region delimited by the electrodes, there is a maximum conductivity value assigned to the lungs' region of 1.713 S/m and a minimum value located in the heart region of 0.274 S/m. This corresponds respectively to relative errors of 2.11 % and 31.5 %. Although the first error is perfectly acceptable, the second one is not. This discrepancy of errors can perhaps be explained by the fact that the true conductivity value assigned to the lungs is much closer

to that of the training targets and hence the algorithm may be more tuned to represent higher conductivity objects than lower conductivity ones. However, the locations of the virtual heart and lungs are well approximated by the reconstruction.

## 4 Conclusion

Concerning the forward problems, the results obtained are in accordance with the consulted bibliography and give some validation to the developed software. However, for both cases, analytical validations are still required in order to have a quantitative measurement of the numerical errors introduced.

Specifically for the MIT case, the next step after this analytical validation consists in connecting the forward problem solver to a 3D modeling program based on a graphical user interface in order to take the developed software a step closer to a commercial version. Also in the MIT case, it is desirable to expand the used formulation to include multi-harmonic signals. The usage of this kind of signals in the source would allow the reconstruction of the conductivity map for different frequencies, which in theory could enhance the contrast and the spatial resolution, since the electromagnetic properties of the tissues varies with the frequency.

In the case of the MIT inverse problem, due to the fact that only the phase shifts information is used, the characterization of the passive electromagnetic properties of the object is compromised since there is only information about the absolute value of the conductivity but not its real and imaginary components. Therefore, the application of the Filtered Back-Projection algorithm to a biological sample would render insufficient results for the clinical application of this technology. Hence, new image reconstruction algorithms need to be developed and tested.

A very interesting thing to study would be the feasibility of the application of the GREIT to the MIT. If it was possible its application to experimental data would be much easier than in the EIT case, since the problem of modeling the contact impedance in the skin-electrode interface would not be present. It re-

mains to test every image reconstruction algorithm on simulated noisy measurements and on experimental data.

## References

- [1] A Korjenevsky et al., "Magnetic induction tomography: experimental realization", *Physiological Measurements*, vol. 21, pp. 89-94, 2000
- [2] Griffiths H, et al., "Magnetic induction tomography: a measuring system for biological tissues", *Ann. New York Acad. Sci.*, vol. 873, no. 3, pp.35-45, 1999
- [3] Robert Merwa and Hermann Scharfetter, "Magnetic induction tomography: comparison of the image quality using different types of receivers", *Physiol. Meas.*, vol. 29, pp. 417-429, 2008.
- [4] M. Soleimani and W. R. B Lionheart, "Absolute Conductivity Reconstruction in Magnetic Induction Tomography Using a Nonlinear Method", *IEEE Transactions on Medical Imaging*, vol. 25, no. 12, pp. 1521-1530, December 2006
- [5] Barber *et al.*, "Electrical Impedance Tomography", *United States Patent*, no. 5,626,146, May 6, 1997
- [6] Brown BH, Seager AD. "The Sheffield data collection system", *Clin. Phys. Physiol. Meas.*, 1987
- [7] Webster JG., "Electrical Impedance Tomography". *Bristol/New York: Adam Hilger*, 1990
- [8] R.H. Bayford, "Bioimpedance Tomography (Electrical Impedance Tomography)", *Annu. Rev. Biomed. Eng.*, 2006
- [9] D. Holder, "Part 1 of Electrical Impedance Tomography: Methods, History and Applications", *Institute of Physics Publishing*, pp. 3-64, 2004
- [10] Geddes LA, Baker LE. 1967. "The specific resistance of biological materials: a compendium of data for the biomedical engineer and physiologist", *Med. Biol. Eng.*, vol. 5, pp. 271-293
- [11] N. B. Bandeira, "Magnetic Induction Tomography - New Approaches Towards a Higher Resolution Biomedical Imaging System", Doctoral Program In Electrical and Computer Engineering, 2009
- [12] M. Clemens and T. Weiland, "Discrete electromagnetism with the finite integration technique", *Progress In Electromagnetics Research*, PIER 32, pp. 65-87, 2001
- [13] J. Junak and U. V. Rienen, "Application of Conformal FIT for Eddy Current Calculation in Coils of a Superconducting Magnet System", *IEEE Transactions on Magnetics*, vol. 40, no 2. pp. 671-674, March 2004
- [14] A. Adler, J. Arnold, R. Bayford, A. Borsic, B. Brown, P. Dixon, T. Faes, I. Frerichs, H. Gagnon, Y. Garber, B. Grychtol, G. Hahn, W. Lionheart, A. Malik, R. Patterson, J. Stocks, A. Tizzard, N. Weiler, G. Wolf, "GREIT: a unified approach to 2D linear EIT reconstruction of lung images", 2009
- [15] J. Mueller, S. Siltanen and D. Isaacson, "A Direct Reconstruction Algorithm for Electrical Impedance Tomography"